Human Molecular Genetics, 2005, Vol. 14, No. 16 **2323–2333**
doi:10.1093/hmg/ddi235
Advance Access published on July 6, 2005

Alms1-disrupted mice recapitulate human Alström syndrome

G.B. Collin[1], E. Cyr[1], R. Bronson[1,2], J.D. Marshall[1], E.J. Gifford[1], W. Hicks[1], S.A. Murray[1], Q.Y. Zheng[1,3], R.S. Smith[1], P.M. Nishina[1] and J.K. Naggert[1,*]

[1]The Jackson Laboratory, 600 Main Street, Bar Harbor, ME 04609, USA, [2]Harvard Medical School, Boston, MA, USA and [3]Department of Physiology, Key Laboratory of Environment and Genes Related Diseases, Xi'an Jiaotong University School of Medicine, Xi'an 710061, China

Received May 14, 2005; Revised June 15, 2005; Accepted June 28, 2005

Mutations in the human *ALMS1* gene cause Alström syndrome (AS), a progressive disease characterized by neurosensory deficits and by metabolic defects including childhood obesity, hyperinsulinemia and Type 2 diabetes. Other features that are more variable in expressivity include dilated cardiomyopathy, hypertriglyceridemia, hypercholesterolemia, scoliosis, developmental delay and pulmonary and urological dysfunctions. *ALMS1* encodes a ubiquitously expressed protein of unknown function. To obtain an animal model in which the etiology of the observed pathologies could be further studied, we generated a mouse model using an *Alms1* gene-trapped ES cell line. *Alms1*$^{-/-}$ mice develop features similar to patients with AS, including obesity, hypogonadism, hyperinsulinemia, retinal dysfunction and late-onset hearing loss. Insulin resistance and increased body weight are apparent between 8 and 12 weeks of age, with hyperglycemia manifesting at ~16 weeks of age. In addition, *Alms1*$^{-/-}$ mice have normal hearing until 8 months of age, after which they display abnormal auditory brainstem responses. Diminished cone ERG b-wave response is observed early, followed by the degeneration of photoreceptor cells. Electron microscopy revealed accumulation of intracellular vesicles in the inner segments of photoreceptors, whereas immunohistochemical analysis showed mislocalization of rhodopsin to the outer nuclear layer. These findings suggest that ALMS1 has a role in intracellular trafficking.

INTRODUCTION

Alström syndrome (AS) [ALMS, Online Mendelian Inheritance in Man (OMIM) no. 203800] is a genetically homogeneous and progressive disorder characterized by cardinal features including cone–rod dystrophy, neurosensory hearing loss, early childhood obesity and insulin resistance leading to Type 2 diabetes (1–3). Other features such as dilated cardiomyopathy, hepatic and urinary dysfunctions and developmental delay are also commonly observed in patients with AS (4).

Recently, mutations in human *ALMS1*, a novel gene of unknown function on chr 2p13, were identified as the basis of AS (5,6). The mutations reported so far have been nonsense and/or frameshift mutations found in exons 8, 10 and 16 (5–9). *ALMS1* has an open reading frame of 4169 amino acids with no sequence homology to other genes. It is ubiquitously expressed, and several splice variants have been identified (5). An interesting structural feature is a large 5 kb exon composed of 34 imperfect repeats of a 47 amino acid motif, which does not bear resemblance to other reported motifs, and its functional significance is not known.

Phenotypically, ALMS strongly resembles another genetically heterogeneous group of disorders, the Bardet–Biedl syndrome (BBS), (OMIM no. 209900). However, the presence of polydactyly and mental retardation in most forms of BBS distinguishes BBS from ALMS. Considerable progress has been made in elucidation of the molecular defects in BBS (10). Eight BBS loci have been identified, and several BBS proteins have recently been linked to basal body function and transport in ciliated cells (11–15). The phenotypic similarities between the two syndromes and the fact that the ALMS protein was identified as a component of the human centrosome (16) make it likely that ALMS acts in the same or related pathways as the BBS proteins.

*To whom correspondence should be addressed. Tel: +1 2072886382; Fax: +1 2072886079; Email: jkn@jax.org

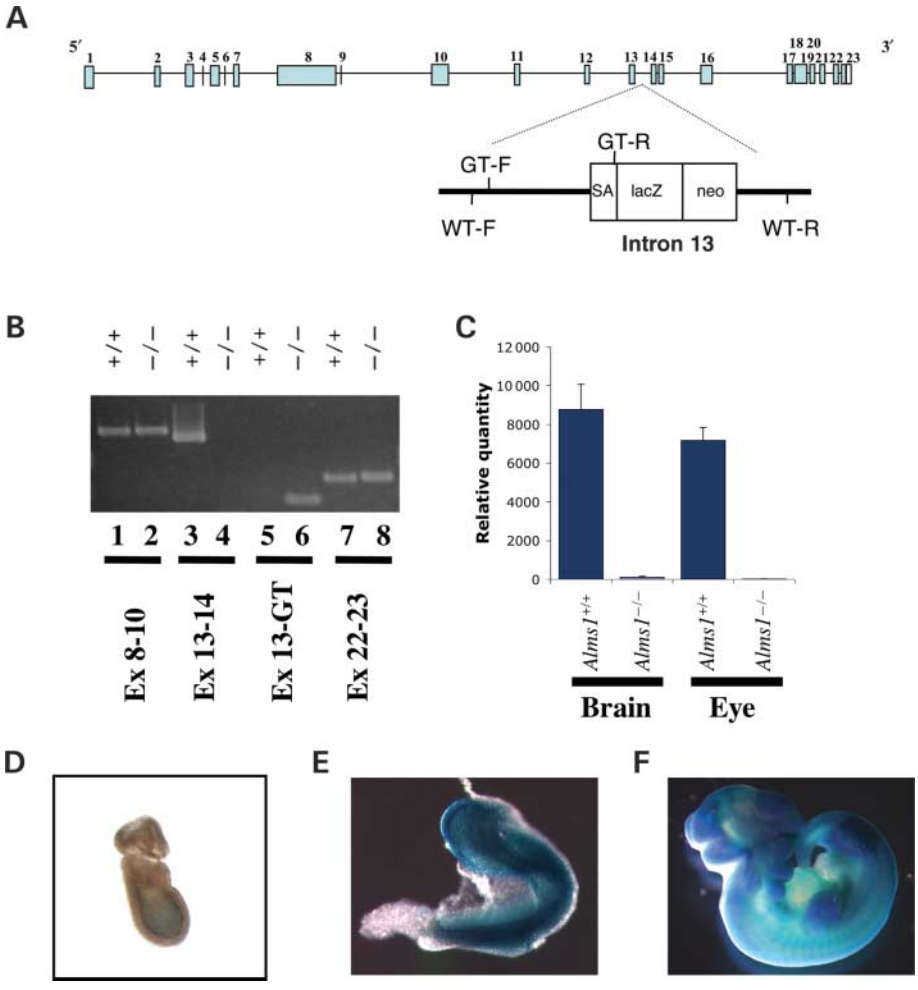

Figure 1. Expression of *Alms1* in normal and mutant mice. (**A**) Insertion site of the gene-trap cassette in intron 13 of the *Alms1* gene (BayGenomics, XH152). Locations of PCR primers for genotyping the mice are shown. The presence of the wild-type allele (399 bp) and/or gene-trap allele (447 bp) can be detected with primer pairs WT-F (5′-TGCAATTATGCCTGCATGC-3′) and WT-R (5′-GTTGACCTGGGGAAGGCT-3′) and GT-F (5′-GATCTTATGAGTCACCATATG-3′) and GT-R (5′-GGACTAACAGAAGAACCCGTT-3′), respectively. (**B**) RT–PCR results of mutant ($Alms1^{-/-}$) and wild-type ($Alms1^{+/+}$) eye cDNA. *Lanes 1 and 2*: cDNA was amplified with oligonucleotides specific for exon 8 and exon 10. *Lanes 3 and 4*: cDNA was amplified with oligonucleotides specific for exon 13 and exon 16. *Lanes 5 and 6*: cDNA was amplified with oligonucleotides specific for exon 13 and the gene-trap. *Lanes 7 and 8*: cDNA was amplified with oligonucleotides specific for exons 22–23, respectively. (Primer locations are shown in Fig. A). By RT–PCR, we observed amplification of exons 22–23, suggesting alternative splicing. (**C**) Real-time PCR results of mutant ($Alms1^{-/-}$) and wild-type ($Alms1^{+/+}$) cDNA. In brain, *Alms1* disruption may have resulted in a hypomorphic allele as demonstrated by a low level of exons 13–14 amplicons in the gene-trap mice. By both RT–PCR and real-time PCR, evidence of normal splicing of exons 13–14 was not observed in eye cDNA. (**D**–**F**) βgal expression in a 7.5-day-old (D), an 8-day-old $Alms1^{+/-}$ heterozygous (E) and a 10.5-day-old $Alms1^{-/-}$ homozygous (F) embryo.

Here, we report a gene-trapped mouse model for AS, $Alms1^{GT(pGT1Lxf)/Pjn}$, which exhibits phenotypic features resembling those of ALMS patients, including obesity, hyperinsulinemia, testicular atrophy and cochlear and retinal degeneration.

RESULTS

Genomic characterization of the gene-trapped *Alms1* locus

DNA prepared from the BayGenomics ES cell line, XH152 (17), was used to determine the gene-trap insertion site. Analysis of 5′-RACE product sequence obtained with a primer specific to *lac* Z showed that the gene was trapped downstream of exon 13. Sequence analysis revealed the insertion site to be in intron 13, 1.97 kb downstream of exon 13. Oligonucleotides for diagnostic PCR were designed to distinguish the $Alms1^{+/+}$ wild-type versus $Alms1^{-/-}$ trapped alleles (Fig. 1A). The genotypic ratio of F2 progeny, i.e. homozygous ($Alms1^{-/-}$) or heterozygous ($Alms1^{+/-}$) for the gene trap and homozygous wild-type ($Alms1^{+/+}$), was 110:229:139, not significantly different from the expected 1:2:1 Mendelian ratio ($P = 0.11$).

The mutation in this model, which would result in a prematurely terminated protein, mimics the most commonly found mutations in the human AS, i.e. premature terminations in the 3′ half of the gene (5–7,9). Such truncations of the messages originating upstream of the last exon typically result in

loss of mRNA due to nonsense mediated decay (18). To assess whether normal *Alms1* splicing of exon 13 into exon 14 was still occurring despite the gene-trap insertion, we isolated total RNA from eye and brain tissue of wild-type and mutant mice. RT–PCR using *Alms1* primers upstream of the gene-trap cassette (exons 8–10) showed strong expression in both $Alms1^{-/-}$ and $Alms1^{+/+}$ mice, whereas downstream expression (using exon 13 and exon 16-specific primers) was not detectable in homozygotes by RT–PCR (Fig. 1B). However, slight traces of normally spliced exon 13–14 cDNA were detected in mutant brain by real-time PCR (Fig. 1C). As we do observe *Alms1* mRNA species containing exons upstream and downstream of the gene trap, ALMS1 isoforms, which have been previously described (5), may exist and the mutation described here may represent a hypomorphic allele.

ALMS1 is present during early development

The *Alms1* gene-trapped allele, $Alms1^{GT(pGT1Lxf)/Pjn}$, expresses a beta-galactosidase (βgal) reporter gene. As some patients with AS display retinal and cardiac pathologies soon after birth, we determined the temporal and spatial localization of ALMS1 during early development using βgal as a marker for *Alms1* expression. Uniform βgal expression was detected as early as embryonic day 7.5 throughout the embryo proper but was absent from the extra-embryonic lineages. At E8.0, βgal expression was found ubiquitously in mesodermal- and ectodermal-derived layers. By E10.5, *Alms1* expression becomes predominant in the mid- and hindbrain and in the fore- and hind limbs (Fig. 1D–F). Expression remains consistent throughout embryonic stages E15.5–E18.5 (data not shown). No obvious developmental abnormalities were observed in the embryos examined, and homozygous mutant offspring are obtained from heterozygote matings in the expected Mendelian ratio.

$Alms1^{-/-}$ mice are obese and males develop Type 2 diabetes

In human patients with AS, one of the earliest clinical manifestations is rapid weight gain in infancy, which progresses to childhood obesity. In $Alms1^{-/-}$ mice (Fig. 2A), body weight begins to increase between 8 and 12 weeks of age when compared with $Alms1^{+/+}$ or $Alms1^{+/-}$ controls. Both female and male $Alms1^{-/-}$ mice have significantly higher body weights than their gender-matched littermates (Fig. 2B and C). The weight of white adipose tissue in individual fat pads was significantly greater in $Alms1^{-/-}$ mice compared with littermate controls (Table 1). The majority of adipose tissue was found in the subcutaneous and reproductive regions. The accumulation of adipose tissue was most notable in female mutants. Adiposity indices in female $Alms1^{-/-}$ mice were 3-fold higher than in controls, whereas affected male mice had adiposity indices that were only 2-fold higher than their lean littermate controls.

Plasma glucose (PG) levels measured between 4 and 24 weeks of age showed that mean PG levels were slightly elevated in both $Alms1^{-/-}$ males and females when compared with control mice. However, overt diabetes (PG $>$ 250 mg/dl) was observed only in affected males after ~16 weeks of age (Fig. 2D and E). All male and female $Alms1^{-/-}$ mice were hyperinsulinemic when tested at 20 weeks of age (Fig. 3A). The hyperinsulinemia in $Alms1^{-/-}$ mutants develops between 8 and 12 weeks of age (data not shown). In addition, although $Alms1^{-/-}$ mice had moderately elevated levels of plasma total cholesterol, plasma triglyceride levels were comparable to controls at 20 weeks of age (Fig. 3B and C).

Multiple organ pathologies in $Alms1^{-/-}$ mice

Livers of both male and female $Alms1^{-/-}$ mice were significantly heavier than those of their heterozygous and wild-type littermates (Table 1). Histologic evaluation of hematoxylin and eosin (H&E) stained Bouin's fixed tissue from 24–30-week-old mutant mice (Fig. 4A) revealed macro- and microvesicular lipid deposits in the liver. The islets in the pancreas were severely enlarged and hyperplastic. Aldehyde fuchsin staining of islets showed granulated islet beta cells but partial degranulation compared with wild-type (Fig. 4B).

Hypogonadism was observed in all $Alms1^{-/-}$ mice compared with the control littermates. Atrophic seminiferous tubules were observed in male testes. Although the degree varied among animals; some testis had severe vacuolization with no secondary spermatocytes (Fig. 4C,D), whereas other testes had normal meiotic I cells with no mature sperms (data not shown).

Kidneys of $Alms1^{-/-}$ mice were enlarged and weighed nearly twice as much as in their wild-type littermates [mean average; 0.37 g per kidney in mutant ($n = 5$) and 0.22 g per kidney in littermates ($n = 9$)] at 6 months of age. Histopathological analysis of H&E stained sections showed dilation of the renal proximal tubules, which contained an eosin-positive, flocculent material of unknown origin (Fig. 4E). Interstitial inflammation and vacuolization, suggestive of degenerating tubules, were observed in a 24-week-old mutant (data not shown). Urinalysis revealed the presence of albumin in male, but not female mutants. Fifty percent of the males had abnormal creatinine:albumin ratios ($>$30), levels indicative of micro- and macro-albuminuria, whereas the females had normal ratios. By light microscopy, we more frequently observed large pyramidal-shaped calcium oxalate diphosphate crystals in the urine sediments of $Alms1^{-/-}$ mice when compared with controls.

$Alms1^{-/-}$ have retinal and cochlear defects

Light stimuli of increasing intensity on a rod-desensitizing background revealed reduced b-wave responses in 24-week-old $Alms1^{-/-}$ mice when compared with their wild-type littermates (Fig. 5A and B). Reduced cone b-wave responses were observed as early as 9 weeks of age. At 24 weeks, the majority of mutant mice show normal dark-adapted ERGs, whereas 33% of mutants show a significantly reduced b-wave amplitude. Retinas from 24-week-old $Alms1^{-/-}$ mice showed loss of cell bodies in the outer nuclear layer (ONL) from ten to six layers and shortening of the inner and outer segments in the majority of the mutants examined (Fig. 5C and D). Additionally, in retinas from 7 and

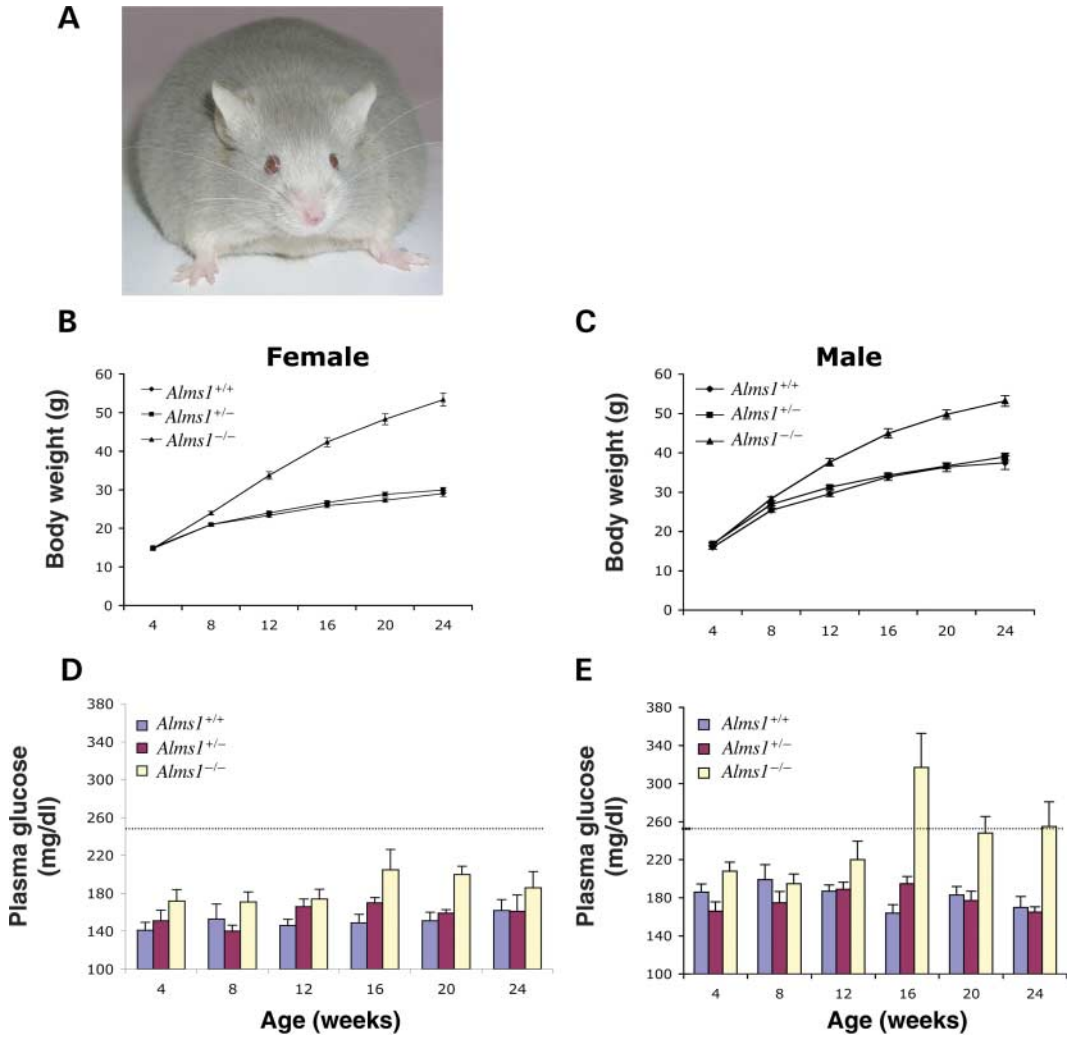

Figure 2. Measures of obesity and diabetes in normal and mutant mice. (**A**) Truncal obesity in a 20-week-old *Alms1*$^{-/-}$ mutant mouse. (**B–E**) Body weight and PG measurements in normal and mutant mice between 4 and 24 weeks of age. Growth curves are shown for female (B) and male (C) homozygous (*Alms1*$^{-/-}$; males $n = 21–53$, females $n = 25–56$), heterozygous (*Alms1*$^{+/-}$; males $n = 35–85$, females $n = 49–102$) and wild-type (+/+; males $n = 33–48$, females $n = 27–43$) mice, where n is the number of mice weighed per time point. PG levels are shown for female (D) and male (E) *Alms1*$^{+/+}$, *Alms1*$^{+/-}$ and *Alms1*$^{-/-}$. Sample sizes for PG were four to 13 animals for each subgroup. Dashed lines represent mean levels indicating transient diabetes. All values are mean ± SEM.

Table 1. Necropsy results of F2 progeny

	Females			Males		
	Alms1$^{-/-}$	*Alms1*$^{+/-}$	*Alms1*$^{+/+}$	*Alms1*$^{-/-}$	*Alms1*$^{+/-}$	*Alms1*$^{+/+}$
Body weight	60.0 ± 4.9	27.5 ± 1.4	26.9 ± 2.0	56.2 ± 6.2	37.4 ± 2.3	39.7 ± 2.7
Total fat	17.6 ± 2.5	2.9 ± 0.8	1.9 ± 0.9	11.3 ± 1.5	3.5 ± 0.8	4.6 ± 1.0
Subcutaneous	6.5 ± 0.4	1.3 ± 0.3	0.9 ± 0.2	5.2 ± 0.5	1.3 ± 0.3	2.3 ± 0.5
Reproductive	5.9 ± 1.8	0.9 ± 0.3	0.6 ± 0.1	2.8 ± 0.7	1.3 ± 0.3	1.3 ± 0.3
Mesenteric	2.2 ± 0.6	0.3 ± 0.1	0.2 ± 0.1	1.5 ± 0.4	0.5 ± 0.1	0.5 ± 0.1
Retroperitoneal	2.2 ± 0.2	0.3 ± 0.1	0.3 ± 0.1	1.6 ± 0.2	0.4 ± 0.1	0.4 ± 0.1
Pericardial	0.4 ± 0.2	Neg	Neg	0.3 ± 0.1	Neg	Neg
Adiposity index*	29.0 ± 2.1	10.2 ± 2.3	6.8 ± 1.0	19.9 ± 0.5	8.9 ± 2.0	11.1 ± 2.1
Liver weight	3.9 ± 0.2	1.2 ± 0.2	1.4 ± 0.2	4.2 ± 0.7	1.8 ± 0.2	1.8 ± 0.2

Numbers represent averages (grams) ± SEM. Necropsies were done on four to five mice from each subgroup. *Adiposity is defined as the percentage of the sum of individual fat pad weights divided by the body weight. Neg, neglible adipose around the heart.

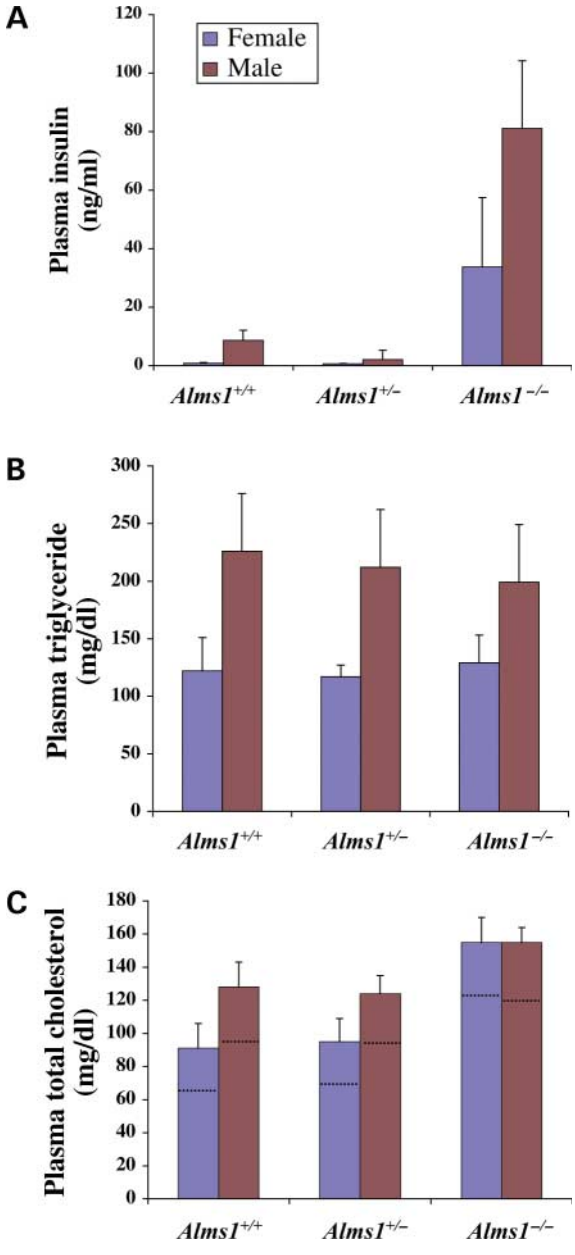

Figure 3. Plasma insulin and lipid measurements in 20-week-old male and female $Alms1^{+/+}$, $Alms1^{+/-}$ and $Alms1^{-/-}$ mice, respectively. (**A**) Both male and female mutants exhibit hyperinsulinemia. (**B**) Plasma concentrations of triglyceride in the mutant and control mice did not differ from controls. (**C**) Plasma total cholesterols are slightly elevated in mutants (HDL levels are indicated by dotted lines). Sample sizes were five to nine animals for each subgroup. Bar graphs are mean ± SEM.

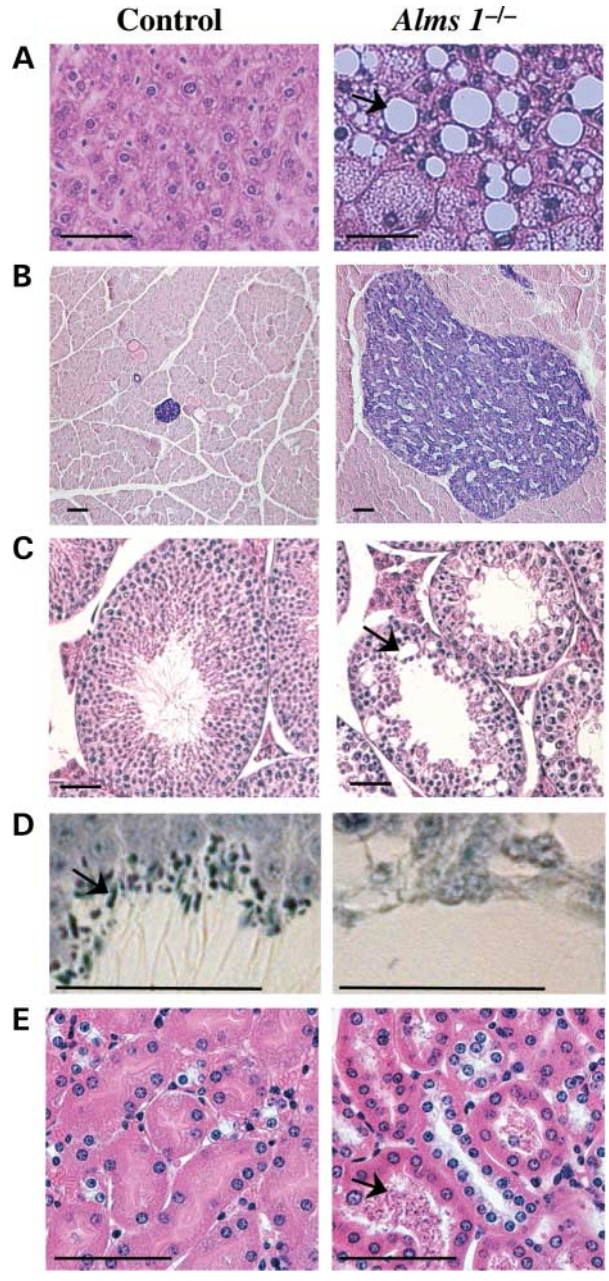

Figure 4. Light micrographs of affected tissues in $Alms1^{-/-}$ mice; controls (left) and mutant (right). H&E (**A**, **C**, **E**), aldehyde fuchsin (**B**), and toluidene blue (**D**). (A) Macro and micro-vesicular lipid deposits (black arrow) accumulate in the liver of a 25-week-old $Alms1^{-/-}$ mouse. (B) Hyperplastic islet is shown in the pancreas of a 24-week-old $Alms1^{-/-}$ mouse. Immunostaining shows an enlarged islet containing insulin-positive beta cells. (C) The testis of the mutant has atrophic seminiferous tubules. Vacuoles (black arrow) are shown surrounding secondary spermatocytes. (D) Sperm heads, stained with toluidene blue in controls (black arrow), are not present in the mutant. (E) Proximal tubules in the mutant kidney are dilated and contain an unidentified flocculent material (black arrow). Scale bars = 50 μm.

24-week-old mutant retinas, a mislocalization of rhodopsin to the ONL was observed (Fig. 5E–G). No evidence of mislocalization was observed with the cone opsins and ROM1 (data not shown), suggesting the defect may be specific to rhodopsin trafficking. Rhodopsin accounts for at least 90% of the protein content in rod photoreceptor discs (19) and thus for a large fraction of the transport across the photoreceptor cilium. Mislocalization of other transported proteins may, therefore, be more difficult to detect and can presently not be ruled out. By electron microscopy, intracellular membrane-bound vesicles were found to accumulate in the distal portion of the inner segments near the connecting cilium of $Alms1^{-/-}$ mice (Fig. 5H–J).

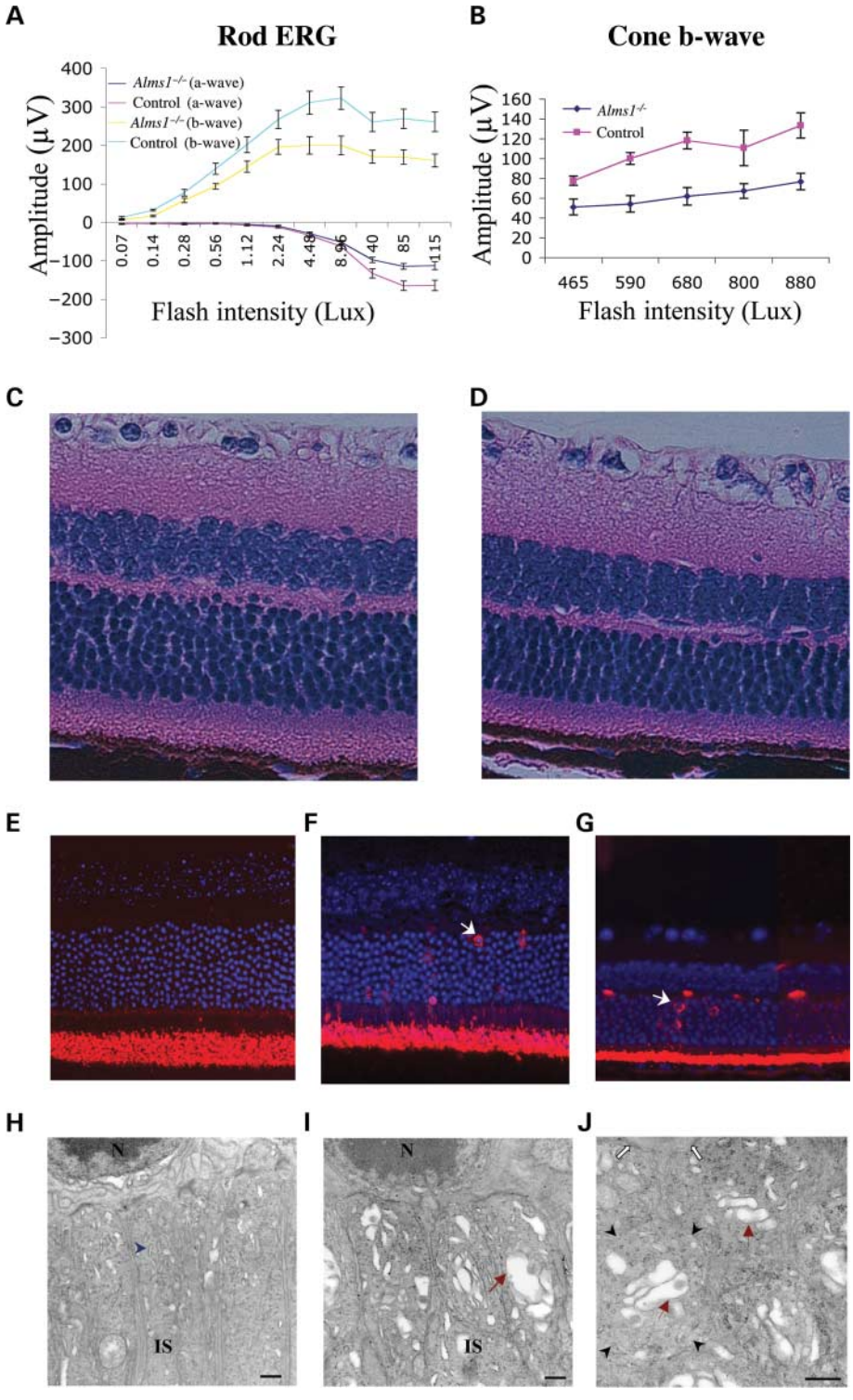

Figure 5. Retinal degeneration in *Alms1*$^{-/-}$ mice. (**A** and **B**) Plots of mean amplitudes (±SEM) versus intensity of dark and light adapted electroretinograms of 24-week-old wild-type and mutant mice (*Alms1*$^{-/-}$, $n = 7$; littermate controls, $n = 7$). Rod and cone b-wave amplitudes are reduced significantly in *Alms1*$^{-/-}$ mice. H&E stained retinal sections of (**C**) 24 week wild-type retina and (**D**) 24-week-old *Alms1*$^{-/-}$ mutant retinas (10×). (**E**–**G**) Rhodopsin localization by fluorescent microscopy of retinas tagged with Cy-3 and anti-rhodopsin. (E) 7-week-old wild-type, (F) 7-week-old mutant and (G) 24-week-old mutant (20×). White arrows show the mislocalization of rhodopsin to the outer segments in *Alms1*$^{-/-}$ mice. (**H**–**J**) Ultrastructural analysis of the outer retina. (H) C57BL/6J wild-type adult mouse retina. Typical rough-surfaced endoplasmic reticulum (blue arrowhead) in the inner segments (IS) consists of small, flattened sacs. N indicates the nucleus of ONL. (I and J) Adult *Alms1*$^{-/-}$ mouse retina. Intracellular vesicles (red arrows) are observed throughout the inner segments, forming stacks resembling the Golgi apparatus. At higher magnification, orientation of the inner segments appears consistently disturbed, often yielding cross-sections (black arrowheads). The white arrows indicate the external limiting membrane and the edge of a photoreceptor nucleus provides orientation. Scale bars (H–J) = 500 nm.

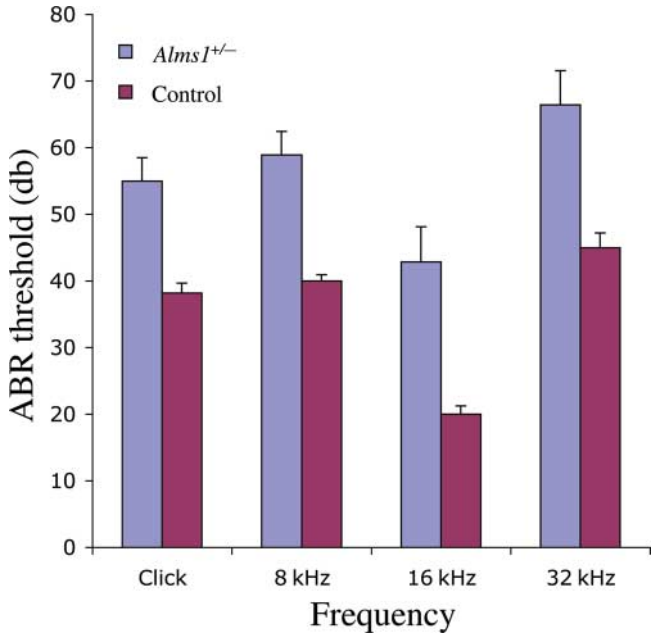

Figure 6. Hearing loss in $Alms1^{-/-}$ mice. At ages between 8 and 12 months, ABR thresholds are higher at all frequencies in $Alms1^{-/-}$ mice ($n = 14$) when compared with their littermates ($n = 11$), indicating hearing impairment across the acoustic spectrum.

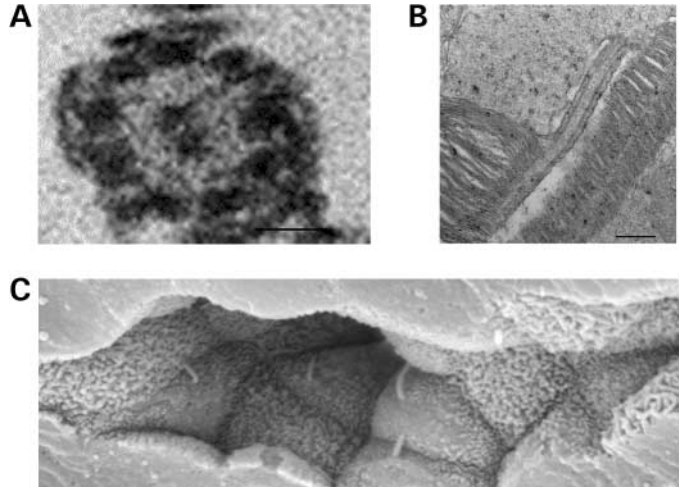

Figure 7. Ultrastructural analysis of motile and primary cilia in $Alms1^{-/-}$ mice. (**A**) Cross-section of motile cilia from the nasal epithelium in an $Alms1^{-/-}$ mouse shown by TEM. The microtubule architecture (9+2 arrangement) of the cilia appears normal. (**B**) Connecting cilia of mutant retina appear intact and are assembled in a typical '9+0' arrangement (data not shown). (**C**) SEM of primary cilia from renal collecting tubules in an $Alms1^{-/-}$ mouse indicates normal cilia formation.

To assess hearing, auditory brainstem response (ABR) analysis was performed at various time points between 1 and 12 months of age. Until 8 months of age, $Alms1^{-/-}$ mice have normal click ABR thresholds. In $Alms1^{-/-}$ mice, 8 months and older, thresholds are >55 db SPL (sound pressure level) and show abnormal ABR thresholds for all sound stimulations: click and 8, 16 and 32 kHz (Fig. 6). By light microscopy, the architecture and layering of the inner and outer hair cells in the middle turn of the organ of corti of 13-month-old hearing impaired mutant mice ($n = 2$) appear normal (data not shown).

$Alms1^{-/-}$ mice assemble cilia normally

To determine whether $Alms1^{-/-}$ assemble normal cilia, motile and primary cilia were examined by ultrastructural analyses. By transmission electron microscopy (TEM), ciliated cells from the nasal epithelium appear normal. Cross-sections of cilia revealed a typical '9+2' microtubule arrangement (Fig. 7A). Connecting cilia in retina from 6-month-old homozygous mutant mice were present, and microtubules were arranged in a normal '9 + 0' fashion (Fig. 7B). By scanning electron microscopy (SEM), primary cilia of renal collecting tubules appear normal in size and number (Fig. 7C).

DISCUSSION

In this study, we show that *Alms1*-disrupted mice recapitulate many of the clinical features of the human syndrome. Obesity, hyperinsulinemia, hypogonadism, retinal degeneration and renal dysfunction parallel those observed in the human syndrome. Similar to individuals with AS, the onset of hyperinsulinemia in mice occurs early; whereas only males become hyperglycemic. Gender bias for Type 2 diabetes is typically observed in mouse models (20). Pancreatic islets show marked hyperplasia associated with beta cell proliferation. This suggests that both insulin resistance and increased insulin secretion may contribute to the glucose intolerance observed.

When compared with the disease progression in human ALMS patients, some differences with respect to the onset and disease progression were observed in our mouse model. For instance, obesity is one of the earliest manifestations observed in human patients, usually presenting by the first year of life (1). In contrast, prepubertal $Alms1^{-/-}$ mice (4-week-old) tend to have lower body weights than their wild-type littermates, and the obesity manifests after puberty, between 8 and 12 weeks of age.

The deduced amino acid sequence of the ALMS1 protein has no similarity to other proteins with known function, nor does the protein sequence contain previously recognizable characterized domains. The first insight into ALMS1 function comes from the findings of Andersen *et al.* (16) who identified ALMS1 as a constituent of centrosomes, microtubule organizing centers that assemble the mitotic spindle and organize the microtubule scaffold, which guides organelle and vesicle trafficking (21). Additionally, in a recent study, ALMS1 was shown to localize to the basal bodies of ciliated cells as well as to the centrosomes (22). Basal bodies anchor the microtubular axoneme of cilia and flagella and help organize intraflagellar transport (23). In recent years, a role for these structures in human disease has become more evident (24). Particularly, the proteins associated with diseases that are phenotypically similar to ALMS, such as BBS, also localize to the centrosomal regions and within the basal bodies of ciliated cells, and studies of mouse models for BBS ($Bbs1^{-/-}$, $Bbs2^{-/-}$, $Bbs4^{-/-}$ and $MKKS^{-/-}$) have implicated several BBS

proteins in ciliary function and intracellular trafficking (12,15,25,26).

Ultrastructural analyses of ciliated cells in *Alms1*$^{-/-}$ mice reveal that cilia undergo normal assembly. However, disruption of the *Alms1* gene in the retina results in the accumulation of large membrane-bound vesicles within photoreceptor inner segments and mislocalization of rhodopsin to the outer segments. Normally, rhodopsin-containing vesicles fuse with the cell membrane at the base of the connecting cilium of photoreceptor cells, and rhodopsin is transported to the photoreceptor outer segments along the cell membrane by an intraflagellar transport system (27). The abnormal accumulation of vesicles in the photoreceptor inner segments in *Alms1*$^{-/-}$ mice indicates a potential role of ALMS1 in ciliary function, perhaps in the process that brings rhodopsin vesicles to the base of the cilium, the docking of the vesicles to the membrane or the attachment of cargo to the intraflagellar transport machinery. A similar retinal phenotype is also observed in null mice deficient in the BBS4 protein, which has also been implicated in the formation and function of flagella (12).

It is interesting to note that the retina of *ALMS1*$^{-/-}$ mice closely resembles that of tubby and *Tulp1*$^{-/-}$ mice whose outer segments form normal disc membranes, which eventually degenerate. In several retinal degeneration models including tubby and *Tulp1*$^{-/-}$ mice, rhodopsin-containing vesicles accumulate in the inner segments (12,28–31). Phenotypically, *Alms1*$^{-/-}$ and tubby (*tub*/*tub*) mice are strikingly similar. Tubby mice exhibit adult-onset obesity and progressive retinal and cochlear degeneration. On specific genetic backgrounds, tubby mice become hyperinsulinemic and males are susceptible to Type 2 diabetes (32). The similarities in clinical features lead us to speculate that ALMS1 and TUB proteins may function in similar biological pathways. Interestingly, the tubby superfamily protein has recently been identified in an analysis of the flagellar and basal body proteome (13), and *Tulp2* was found to be induced during flagellar regeneration in Chlamydomonas (33), further suggesting a role for both TULPs and ALMS1 in cilia related functions.

In conclusion, the *Alms1*$^{-/-}$ mice described here recapitulate the phenotypes observed in patients with AS, including obesity, hyperinsulinemia leading to Type 2 diabetes, hypogonadism and neurosensory deficits. This new model for AS will allow detailed investigation of the disease pathology as well as testing hypotheses about ALMS1 function. Elucidation of the biochemical function of ALMS1 is crucial for a better understanding of the pathogenesis involved in AS as well as in the more common forms of obesity, diabetes and retinal and cochlear degeneration.

MATERIALS AND METHODS

Generation and husbandry of *ALMS1* $^{-/-}$ mice

A 129-derived ES cell line (XH152) (17) containing a gene-trap cassette in the *Alms1* gene was obtained through the Mutant Mouse Regional Resource Center (MMRRC). *Alms1*$^{+/-}$ ES cells were microinjected into blastocysts of C57BL/6J mice. Chimeric males were backcrossed to C57BL/6J and the agouti pups from the F1 progeny were genotyped as described subsequently. *Alms1*$^{+/-}$ heterozygous mice were intercrossed to produce a total of 478 progeny.

Mice, in this study, were bred in the Research Animal Facility at The Jackson Laboratory. Mice were *ad libitum* fed a NIH31 diet with 6% fat (PMI Feeds Inc., St Louis, MO, USA) and provided unlimited access to water (HCl acidified, pH 2.8–3.2) in a temperature and humidity controlled setting with a 12 h light/dark cycle.

Analysis of gene-trap insertion site

Genomic DNA from ES cells XH152 was PCR amplified with an *Alms1* exon 13-specific primer (5′-GATTTATAGCAAGAGGGCTGC-3′) and a gene-trap cassette-specific primer (5′-GGACTAACAGAAGAACCCGTT-3′) using the Expand Template System (Roche). The resulting product of 1.97 kb was subcloned into TOPO XL (Invitrogen) and the plasmid was electrophorated into TOPO electrocompetent cells. Plasmids were purified using the Qiaprep spin columns (Qiagen) and subsequently sequenced with M13F and M13R primers. Sequence alignments were performed using MacVector 6.0 to determine the position of the gene-trap insertion site.

Analysis of mutant cDNA by RT–PCR

Total RNA from a mutant (*Alms1*$^{-/-}$) and wild-type (*Alms*$^{+/+}$) adult brain and eye was isolated using the Trizol method (GIBCO), followed by DNaseI digestion of residual DNA (Ambion). cDNA was made from RNA by RT–PCR (Superscript). PCR was performed on the cDNA using the Expand Template System (Roche) according to the manufacturer's instructions. 5′-RACE of XH152 revealed that the slice donor site of intron 13 was splicing into the splice acceptor site of the gene trap (BayGenomics). Oligonucleotides were designed to amplify regions upstream (exon 8F, 5′-TCCCTATGATGACAATCAT-3′ and exon 10R, 5′-GTGCATTTCTGATTCCTCTGG-3′) and downstream of the insertion site (exon13F, 5′-CACTGTAAACATTAAGCAC-3′ and exon 16R, 5′-GAACACAGCCTGTCCCCAA-3′). Amplification products were separated by electrophoresis on a 2% agarose gel and visualized by ethidium bromide staining under UV illumination.

Real-time PCR with Taqman gene expression assays (Applied Biosystems) was performed according to manufacturer's protocol with an ABI7900HT system. Primer/probes for *Alms1* coding regions spanning the gene trap (exons 13–14) were manufactured by Applied Biosystems' Assay By Design technology. Absolute quantitation expression analysis (34) was performed using eye and brain from three *Alms1*$^{-/-}$ and three *Alms1*$^{+/+}$ biological replicates. For technical validation, all reactions were performed in triplicates. Real-time PCR reactions using known concentrations (10^{-5}, 10^{-4}, 10^{-3}, 10^{-2}, 10^{-1} and 1 ng) of PCR-amplified *Alms1* cDNA products were used as standards. A 'no-template control' was performed as a negative control. Standard curves were generated and absolute expression values were determined. In the figure, the 'no-template control' values were subtracted from the absolute values to generate a 'no expression' baseline. All standard curves were linear.

Genotyping

A forward primer specific to *Alms1* intron 13 upstream of the gene trap (GT-F) and a reverse primer specific to the gene-trap cassette (GT-R) were designed to detect the mutant *Alms1* allele. A forward primer specific to *Alms1* intron 13 upstream of gene trap (WT-F) and a reverse primer specific to *Alms1* intron 13 downstream of the gene trap (WT-R) were used to detect the wild-type allele. The sequences of primers are shown in Figure 1. The PCR conditions were as follows: initial denaturation at 94°C for 2 min, followed by 45 cycles of 94°C for 20 s, 54°C for 30 s and 72°C for 30 s and a final extension of 72°C for 7 min. As the genotypes were based on the presence or absence of bands, the annealing temperature was reduced to allow for non-specific binding such that we could visualize bands in the gene-trap animal (to control for DNA content).

X-gal staining of embryos

Timed matings were performed using $Alms1^{+/-}$ female bred to $Alms1^{+/-}$ male mice. At embryonic days E7.5, E8.0, E10.5, E15.5 and E18.5, pregnant females were sacrificed and embryos were harvested. The yolk sac from each embryo was collected for genotypic analysis. Embryos were fixed in 2% PFA or glutaraldehyde at room temperature for 2 h, rinsed with PBS and then placed in X-gal solution (www.baygenomics.ucsf.edu/protocols/) and incubated at 37°C overnight. Protein expression of whole embryos was visualized by stereomicroscopy for the presence of a blue color.

Biochemical measurements

Mice (N1F2) were weighed monthly until termination at 24 weeks of age. Whole blood was collected via the orbital sinus bi-weekly using EDTA coated capillary tubes. Samples were centrifuged and plasma was used for all biochemical assays. PG, cholesterol and triglyceride levels were measured using a Beckman Coulter Synchron CX5 Delta chemistry analyzer. Plasma insulin levels were measured using an ultrasensitive mouse insulin ELISA kit (ALPCO Diagnostics). PG levels were monitored bi-weekly, whereas lipid and insulin levels were determined at 20 weeks of age and at termination.

Histological and immunohistochemical analysis

Mice (N1F2) were sacrificed by CO_2 asphyxiation and tissues were dissected and placed in Bouin's fixative overnight. Eyes were oriented by cauterization and placed in cold acetic acid/methanol (1:3 ratio) overnight. Tissues embedded in paraffin, using standard procedures, were cut into 6–8 μm sections, stained with H&E or aldehyde fuchsin (pancreas only) and visualized by light microscopy.

For immunohistochemical analysis, retinal sections were de-paraffinized and incubated with 1:500 anti-rhodopsin (Leinco Technologies), 1:500 anti-ROM1, 1:500 anti-blue opsin (Chemicon) and/or 1:500 anti-red/green opsin overnight. After several washes in PBS, sections were incubated with a Cy3-conjugated mouse secondary antibody (Jax Immunoresearch) and stained with DAPI (Sigma) for nuclear staining. Localization of rhodopsin, ROM1, and cone opsins was visualized by fluorescence microscopy.

Electron microscopy

TEM on retina. Mice were sacrificed by CO_2 euthanasia and eyes were immediately removed and fixed in phosphate-buffered gluteraldehyde/paraformaldehyde solution for 3 h at 4°C. Following fixation, the anterior segment was removed and the posterior segment was cut into transverse blocks ($1 \times 2\ mm^2$), including retina, choroid and sclera, and placed in fresh fixative for an additional 2–8 h. Tissues were then post-fixed in 1% osmium tetroxide, dehydrated and embedded in plastic. Tissue sections were cut and stained in uranyl acetate and lead citrate and examined under a TEM.

SEM on kidneys. Kidneys cut longitudinally were fixed in 2.5% gluteraldehyde in cacodylate buffer overnight. Tissues were rinsed twice in cacodylate buffer, dehydrated and freeze fractured with liquid nitrogen. Tissues were then re-hydrated, treated with osmium tetroxide, dehydrated and sputter coated. Specimens were mounted and examined under a SEM.

Fundus evaluation and electroretinograms

Mice were dark-adapted and their pupils dilated with atropine prior to examination by indirect ophthalmoscopy with a 60 or 78 diopter aspheric lens. Fundus photographs were taken with a Kowa fundus camera using a Volk superfield lens held 2 in. from the eye. The highest flash intensity was used with Kodak black and white Tmax 400 ASA professional film for the photodocumentation. The protocol for full field ERGs has been previously described (35). Briefly, a gold loop electrode was placed on the corneal surface at the limbus and referenced to a gold wire placed in the mouth of mice anesthetized with a mixture of xylene/ketamine (7 and 15 mg/gm, respectively). A needle electrode inserted in the tail served as ground. Mice were placed on a 38°C heating pad throughout the procedure. Signals were amplified (×10 000, CP511 AC amplifier, Grass Instruments), sampled every 0.8 ms and averaged. Rod-mediated ERGs were recorded from mice adapted to the dark overnight and exposed to short-wavelength flashes in a Ganzfeld dome, which varied over a 4.0 log unit range of intensities up to the maximum allowable by the photopic stimulator (PS33 Plus, Grass Instruments). Cone-mediated responses were obtained with white flashes on a rod-saturating background after 10 min of light adaptation. Responses were computer averaged at all intensities with up to 50 records averaged for the weakest signals. A signal rejection window was used to eliminate electrical artifacts produced by blinking and eye movements.

Assessment of hearing by ABR

ABRs were conducted as previously described (36). Briefly, mice were anesthetized and their body temperature was maintained at 37–38°C by placing them on a heating pad in the soundproof chamber during testing. Subdermal needle

electrodes were inserted at the vertex (active) and ventrolaterally to the right ear (reference) and the left ear (ground). Specific auditory stimuli (broadband click and pure-tone pips of 8, 16 and 32 kHz) from high-frequency transducers were delivered binaurally through plastic tubes to the ear canals. Evoked brain-stem responses were amplified and averaged and their wave patterns were displayed on a computer screen. Auditory threshold was obtained for each stimulus by varying the SPL at 10 dB steps and finally at 5 dB step up and down to identify the lowest level at which an ABR pattern could be recognized.

ACKNOWLEDGEMENTS

We would like to thank Jay Young, Ian Welch, Elizabeth Hinman, Pete Finger, Drs Noel Murcia, Malia Edwards, Keith DiPetrillo, Akihiro Ikeda and Dennis Maddox for technical assistance and helpful discussions, Douglas Howell for ERG analysis and Drs Ed Leiter and Barbara Knowles for careful review of this manuscript. An anti-ROM1 antibody was a kind gift from Dr McInnes. This work was supported through a grant from the National Institutes of Health, HD36878. Core services were supported by an institutional grant (CA24190) and a Resource grant from the NEI (EY14751).

Conflict of Interest statement. None declared.

REFERENCES

1. Marshall, J.D., Ludman, M.D., Shea, S.E., Salisbury, S.R., Willi, S.M., LaRoche, R.G. and Nishina, P.M. (1997) Genealogy, natural history, and phenotype of Alstrom syndrome in a large Acadian kindred and three additional families. *Am. J. Med. Genet.*, **73**, 150–161.
2. Michaud, J.L., Heon, E., Guilbert, F., Weill, J., Puech, B., Benson, L., Smallhorn, J.F., Shuman, C.T., Buncic, J.R., Levin, A.V. *et al.* (1996) Natural history of Alstrom syndrome in early childhood: onset with dilated cardiomyopathy. *J. Pediatr.*, **128**, 225–229.
3. Alstrom, C.H., Hallgren, B., Nilsson, L.B. and Asander, H. (1959) Retinal degeneration combined with obesity, diabetes mellitus and neurogenous deafness: a specific syndrome (not hitherto described) distinct from the Laurence–Moon–Bardet–Biedl syndrome: a clinical, endocrinological and genetic examination based on a large pedigree. *Acta Psychiatr. Neurol. Scand.*, **34**, 1–35.
4. Marshall, J.D., Bronson, R.T., Collin, G.B., Nordstrom, A.D., Maffei, P., Paisey, R.B., Carey, C., Macdermott, S., Russell-Eggitt, I., Shea, S.E. *et al.* (2005) New Alstrom syndrome phenotypes based on the evaluation of 182 cases. *Arch. Intern. Med.*, **165**, 675–683.
5. Collin, G.B., Marshall, J.D., Ikeda, A., So, W.V., Russell-Eggitt, I., Maffei, P., Beck, S., Boerkoel, C.F., Sicolo, N., Martin, M. *et al.* (2002) Mutations in ALMS1 cause obesity, Type 2 diabetes and neurosensory degeneration in Alstrom syndrome. *Nat. Genet.*, **31**, 74–78.
6. Hearn, T., Renforth, G.L., Spalluto, C., Hanley, N.A., Piper, K., Brickwood, S., White, C., Connolly, V., Taylor, J.F., Russell-Eggitt, I. *et al.* (2002) Mutation of ALMS1, a large gene with a tandem repeat encoding 47 amino acids, causes Alstrom syndrome. *Nat. Genet.*, **31**, 79–83.
7. Bond, J., Flintoff, K., Higgins, J., Scott, S., Bennet, C., Parsons, J., Mannon, J., Jafri, H., Rashid, Y., Barrow, M. *et al.* (2005) The importance of seeking ALMS1 mutations in infants with dilated cardiomyopathy. *J. Med. Genet.*, **42**, e10.
8. Hart, L.M., Maassen, J.A., Dekker, J.M. and Heine, R.J. (2003) Lack of association between gene variants in the *ALMS1* gene and Type 2 diabetes mellitus. *Diabetologia*, **46**, 1023–1024.
9. Titomanlio, L., De Brasi, D., Buoninconti, A., Sperandeo, M.P., Pepe, A., Andria, G. and Sebastio, G. (2004) Alstrom syndrome: intrafamilial phenotypic variability in sibs with a novel nonsense mutation of the *ALMS1* gene. *Clin. Genet.*, **65**, 156–157.
10. Bhogal, A. and Leavitt, B. (2004) Computational biology to the rescue: the ongoing quest to understand Bardet–Biedl syndrome. *Clin. Genet.*, **66**, 296–298.
11. Ansley, S.J., Badano, J.L., Blacque, O.E., Hill, J., Hoskins, B.E., Leitch, C.C., Kim, J.C., Ross, A.J., Eichers, E.R., Teslovich, T.M. *et al.* (2003) Basal body dysfunction is a likely cause of pleiotropic Bardet–Biedl syndrome. *Nature*, **425**, 628–633.
12. Mykytyn, K., Mullins, R.F., Andrews, M., Chiang, A.P., Swiderski, R.E., Yang, B., Braun, T., Casavant, T., Stone, E.M. and Sheffield, V.C. (2004) Bardet–Biedl syndrome type 4 (BBS4)-null mice implicate Bbs4 in flagella formation but not global cilia assembly. *Proc. Natl Acad. Sci. USA*, **101**, 8664–8669.
13. Li, J.B., Gerdes, J.M., Haycraft, C.J., Fan, Y., Teslovich, T.M., May-Simera, H., Li, H., Blacque, O.E., Li, L., Leitch, C.C. *et al.* (2004) Comparative genomics identifies a flagellar and basal body proteome that includes the BBS5 human disease gene. *Cell*, **117**, 541–552.
14. Kim, J.C., Badano, J.L., Sibold, S., Esmail, M.A., Hill, J., Hoskins, B.E., Leitch, C.C., Venner, K., Ansley, S.J., Ross, A.J. *et al.* (2004) The Bardet–Biedl protein BBS4 targets cargo to the pericentriolar region and is required for microtubule anchoring and cell cycle progression. *Nat. Genet.*, **36**, 462–470.
15. Fath, M.A., Mullins, R.F., Searby, C., Nishimura, D.Y., Wei, J., Rahmouni, K., Davis, R.E., Tayeh, M.K., Andrews, M., Yang, B. *et al.* (2005) Mkks-null mice have a phenotype resembling Bardet–Biedl Syndrome. *Hum. Mol. Genet.*, **14**, 1109–1118.
16. Andersen, J.S., Wilkinson, C.J., Mayor, T., Mortensen, P., Nigg, E.A. and Mann, M. (2003) Proteomic characterization of the human centrosome by protein correlation profiling. *Nature*, **426**, 570–574.
17. Stryke, D., Kawamoto, M., Huang, C.C., Johns, S.J., King, L.A., Harper, C.A., Meng, E.C., Lee, R.E., Yee, A., L'Italien, L. *et al.* (2003) BayGenomics: a resource of insertional mutations in mouse embryonic stem cells. *Nucleic Acids Res.*, **31**, 278–281.
18. Schell, T., Kulozik, A.E. and Hentze, M.W. (2002) Integration of splicing, transport and translation to achieve mRNA quality control by the nonsense-mediated decay pathway. *Genome Biol.*, **3**, REVIEWS1006.
19. Hargrave, P.A. and McDowell, J.H. (1992) Rhodopsin and phototransduction: a model system for G protein-linked receptors. *FASEB J.*, **6**, 2323–2331.
20. Schafir, E. (1992) Animal models of non-insulin-dependent diabetes. *Diabetes Metab. Rev.*, **8**, 179–208.
21. Thyberg, J. and Moskalewski, S. (1999) Role of microtubules in the organization of the Golgi complex. *Exp. Cell Res.*, **246**, 263–279.
22. Hearn, T., Spalluto, C., Phillips, V.J., Renforth, G.L., Copin, N., Hanley, N.A. and Wilson, D.I. (2005) Subcellular localization of ALMS1 supports involvement of centrosome and basal body dysfunction in the pathogenesis of obesity, insulin resistance, and Type 2 diabetes. *Diabetes*, **54**, 1581–1587.
23. Rosenbaum, J.L. and Witman, G.B. (2002) Intraflagellar transport. *Nat. Rev. Mol. Cell Biol.*, **3**, 813–825.
24. Badano, J.L., Teslovich, T.M. and Katsanis, N. (2005) The centrosome in human genetic disease. *Nat. Rev. Genet.*, **6**, 194–205.
25. Nishimura, D.Y., Fath, M., Mullins, R.F., Searby, C., Andrews, M., Davis, R., Andorf, J.L., Mykytyn, K., Swiderski, R.E., Yang, B. *et al.* (2004) Bbs2-null mice have neurosensory deficits, a defect in social dominance, and retinopathy associated with mislocalization of rhodopsin. *Proc. Natl Acad. Sci. USA*, **101**, 16588–16593.
26. Kulaga, H.M., Leitch, C.C., Eichers, E.R., Badano, J.L., Lesemann, A., Hoskins, B.E., Lupski, J.R., Beales, P.L., Reed, R.R. and Katsanis, N. (2004) Loss of BBS proteins causes anosmia in humans and defects in olfactory cilia structure and function in the mouse. *Nat. Genet.*, **36**, 994–998.
27. Deretic, D. (1998) Post-Golgi trafficking of rhodopsin in retinal photoreceptors. *Eye*, **12**, 526–530.
28. Hagstrom, S.A., Duyao, M., North, M.A. and Li, T. (1999) Retinal degeneration in tulp1−/− mice: vesicular accumulation in the interphotoreceptor matrix. *Invest. Ophthalmol. Vis. Sci.*, **40**, 2795–2802.
29. Heckenlively, J.R., Chang, B., Erway, L.C., Peng, C., Hawes, N.L., Hageman, G.S. and Roderick, T.H. (1995) Mouse model for Usher syndrome: linkage mapping suggests homology to Usher type I reported at human chromosome 11p15. *Proc. Natl Acad. Sci. USA*, **92**, 11100–11104.

30. Jansen, H.G. and Sanyal, S. (1984) Development and degeneration of retina in rods mutant mice: electron microscopy. *J. Comp. Neurol.*, **224**, 71–84.
31. Li, T., Snyder, W.K., Olsson, J.E. and Dryja, T.P. (1996) Transgenic mice carrying the dominant rhodopsin mutation P347S: evidence for defective vectorial transport of rhodopsin to the outer segments. *Proc. Natl Acad. Sci. USA*, **93**, 14176–14181.
32. Coleman, D.L. and Eicher, E.M. (1990) Fat (fat) and tubby (tub): two autosomal recessive mutations causing obesity syndromes in the mouse. *J. Hered.*, **81**, 424–427.
33. Stolc, V., Samanta, M.P., Tongprasit, W. and Marshall, W.F. (2005) Genome-wide transcriptional analysis of flagellar regeneration in *Chlamydomonas reinhardtii* identifies orthologs of ciliary disease genes. *Proc. Natl Acad. Sci. USA*, **102**, 3703–3707.
34. Prieto-Alamo, M.J., Cabrera-Luque, J.M. and Pueyo, C. (2003) Absolute quantitation of normal and ROS-induced patterns of gene expression: an *in vivo* real-time PCR study in mice. *Gene Expr.*, **11**, 23–34.
35. Nusinowitz, S., Ridder, W.H., III and Heckenlively, J.R. (2002) In Smith, R.S., John, S.W., Nishina, P. and Sundberg, J.P. (eds), *Systematic Evaluation of the Mouse Eve: Anatomy, Pathology, and Biomethods.* CRC, New York, pp. 320–344.
36. Zheng, Q.Y., Johnson, K.R. and Erway, L.C. (1999) Assessment of hearing in 80 inbred strains of mice by ABR threshold analyses. *Hear. Res.*, **130**, 94–107.